Effect of chemical order on the magnetic and electronic properties of epitaxial off-stoichiometry Fe_xSi_{1-x} thin films

J. Karel,[1,2] J. Juraszek,[3] J. Minar,[4,5] C. Bordel,[2,3,6] K. H. Stone,[2] Y. N. Zhang,[7] J. Hu,[7]
R. Q. Wu,[7] H. Ebert,[4] J. B. Kortright,[2] and F. Hellman[1,2,6]

[1]*Department of Materials Science and Engineering, University of California, Berkeley, Berkeley, California 94709, USA*
[2]*Materials Science Division, Lawrence Berkeley National Laboratory, Berkeley, California 94720, USA*
[3]*Groupe de Physique des Matériaux, UMR6634 CNRS-Université de Rouen, F-76801 St. Etienne du Rouvray, France*
[4]*Dept. Chemie und Biochemie, Physikalische Chemie, Universität München, München, Germany*
[5]*New Technologies - Research Center, University of West Bohemia, Univerzitni 8, 306 14 Pilsen, Czech Republic*
[6]*Physics Department, University of California, Berkeley, Berkeley, California 94709, USA*
[7]*Department of Physics and Astronomy, University of California, Irvine, California 92697, USA*

(Received 20 April 2014; published 6 April 2015)

Off-stoichiometry, epitaxial Fe_xSi_{1-x} thin films ($0.5 < x < 1.0$) exhibit $D0_3$ or $B2$ chemical order, even far from stoichiometry. Theoretical calculations show the magnetic moment is strongly enhanced in the fully chemically disordered $A2$ phase, while both theoretical and experimental results show that the magnetization is nearly the same in the $B2$ and $D0_3$ phases, meaning partial chemical disorder does not influence the magnetism. The dependencies of the magnetic moments are directly and nonlinearly linked to the number of Si atoms, primarily nearest neighbor but also to a lesser extent (up to 10%) next nearest neighbor, surrounding Fe, explaining the similarities between $B2$ and $D0_3$ and the strong enhancement for the $A2$ structure. The calculated electronic density of states shows many similarities in both structure and spin polarization between the $D0_3$ and $B2$ structures, while the $A2$ structure exhibits disorder broadening and a reduced spin polarization.

DOI: 10.1103/PhysRevB.91.144402 PACS number(s): 75.50.Bb, 76.80.+y, 71.15.Mb

I. INTRODUCTION

Stoichiometric Fe_3Si, a binary Heusler alloy with $D0_3$ crystal structure shown in Fig. 1(a), is metallic and possesses a high Curie temperature and a large, theoretically predicted spin polarization [1,2]. By taking advantage of vapor deposition techniques, metastable films of Fe_xSi_{1-x} ($x < 0.75$) can be prepared with varying degrees of chemical order, allowing tuning of the magnetic and electronic properties, and thus making the system an attractive material as a potential spin injector. In particular, reducing x leads to a decrease in carrier concentration, which is an important parameter in the physics of magnetic semiconductors quite generally and specifically in the context of the resistivity mismatch when considering spin injection for devices without an oxide tunnel barrier. Thin-film growth is required since in equilibrium, the relevant composition range ($0.50 < x < 0.75$) is the two-phase phase field of $D0_3$ Fe_3Si and ε-FeSi [3]. Stoichiometric ε-FeSi has the $B20$ structure and is considered a "Kondo insulator" with exotic magnetic properties [4]. Similar $B20$ phase materials such as FeGe have a helical ground state at zero field, a ferromagnetic state at high field, and skyrmions at intermediate field and temperature due to Dzyaloshinsky-Moriya interactions, but the magnetic moment in $B20\,\varepsilon-$FeSi is, by contrast, fully quenched [5]. The $D0_3$ crystal structure unit cell has an fcc Bravais lattice and can be thought of as 8-bcc-like subunits with Fe (Fe_{II}) on the cube corners and Fe (Fe_I) and Si alternating in the body centers [6,7]. Fe_{II} is surrounded by four Fe nearest neighbors (NN) and four Si NN and carries a magnetic moment M of $1.35\,\mu_B$ [6]. Fe_I is surrounded by eight Fe NN; M is $2.2\,\mu_B$ [6]. These two sites are chemically inequivalent; our previous work found a clear distinction between the contribution of each site to the valence-band spectra in hard x-ray photoemission spectroscopy [8]. In thin-film form, it is possible, in theory, to fabricate metastable stoichiometric and off-stoichiometric cubic Fe-Si alloys with either the $A2$, $B2$ (CsCl), or the $D0_3$ structure. In the most chemically ordered system (off-stoichiometry $D0_3$), additional Si (Fe) substitutes onto Fe_I (Si) lattice sites [Fig. 1(b)]. Partial ordering occurs in the off-stoichiometry ($x > 0.5$) $B2$ structure, where Fe is ordered at the cube corners (Fe_{II}), but Fe and Si randomly occupy the body center sites (Fe_I combined with Si sites) [Fig. 1(c)]. In the $A2$ structure, there is no long-range chemical ordering, but bcc structural order is maintained.

These varying degrees of chemical order can be used to significantly tune the properties of this Heusler alloy. Experimental work has shown the magnetic properties of bulk Fe_xSi_{1-x} alloys near $x = 0.75$ are strongly dependent on the local atomic environment and Fe concentration [6,9]. Additionally, experimental thin-film studies and theoretical investigations show that the density of states can be tuned by varying the Fe concentration or by doping with small amounts of V, Mn, or Cr [6,7,10,11]. Recent work on another Heusler alloy, Co_2FeSi thin films, has shown a reversal of spin polarization due to differences in the density of states between the ordered $L2_1$ and partially ordered $B2$ structures [12]. Work on Fe_xSi_{1-x} thin films to date has focused on the chemically ordered endpoints of the composition range near $x = 0.75$ or 0.5 [13–17]. Berling *et al.* found a reduction in the magnetic moment with increasing Si concentration and attributed it to increased Si NN around Fe_{II} atoms and a reduction in the total number of Fe_I atoms with decreasing x [6]. However, the local chemical order was not clarified and the electronic structure was not investigated in that work.

In the present work, we fabricated and investigated off-stoichiometry Fe_xSi_{1-x} epitaxial thin films ($0.55 \leqslant x \leqslant 0.77$). Experimentally we found that the material has a strong tendency to chemically order so films with the $A2$ structure

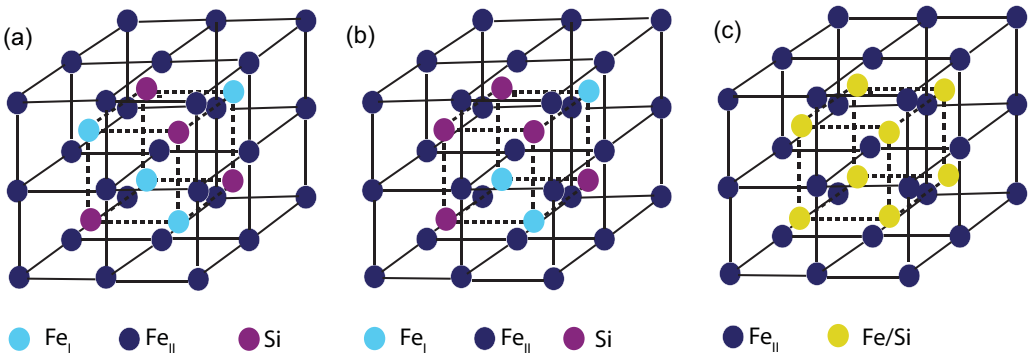

FIG. 1. (Color online) (a) $D0_3$ crystal structure for $x = 0.75$, (b) off-stoichiometry $D0_3$ (e.g., $x = 0.687\,5$ shown here), and (c) $B2$ ($x \geqslant 0.5$). Fe/Si indicates the site is occupied by either Fe or Si, depending on x. For $x = 0.50$ in (c), all the Fe/Si sites are occupied by Si. In the $A2$ structure for all x, all sites in any of these structures (a, b, or c) are occupied by Fe or Si with the probability depending on composition.

were not successfully fabricated, but both $B2$ and $D0_3$ were successfully made and the properties of all structures were theoretically analyzed. Chemical order was characterized using ^{57}Fe conversion electron Mössbauer spectroscopy (CEMS). The electronic and magnetic properties of these materials were investigated theoretically using calculations of the electronic density of states, spin polarization, and magnetic moments, and experimentally by x-ray absorption spectroscopy (XAS) and magnetometry to understand the effects of chemical order on these properties. Our work ultimately shows that partial chemical disorder has very little effect on the magnetic and electronic properties of these materials; significant changes are only observed when the material is fully disordered. This result has important implications for spintronic devices because it confirms the use of metastable off-stoichiometric Fe_xSi_{1-x} films to optimize resistivity and magnetization, without concerns about their chemical disorder.

II. METHODS

A. Theoretical density functional theory calculations

Electronic structure calculations for $D0_3$ Fe_xSi_{1-x} ($x = 0.60$–0.77), $B2$ Fe_xSi_{1-x} ($x = 0.55$–0.67), and $A2$ Fe_xSi_{1-x} ($x = 0.60$–0.80) were performed within the *ab initio* framework of spin-density functional theory. The Vosko, Wilk, and Nusair parametrization of the exchange and correlation potential was used [18]. For all systems, the experimental lattice constants (or a linear extrapolation from experimental values for other x) were used. The electronic structure was calculated in a fully relativistic model by solving the corresponding Dirac equation using the spin-polarized relativistic (SPR) multiple-scattering or Korringa-Kohn-Rostoker (KKR) formalism [19]. To account for electronic correlations beyond the local spin-density approximation (LSDA), a combined LSDA+DMFT (dynamical mean-field theory) scheme was employed, self-consistent in both the self-energy calculation and the charge density calculation, as implemented within the relativistic SPR-KKR formalism [20]. As a DMFT solver, the relativistic version of the so-called spin-polarized T-matrix plus fluctuation (SPTF) exchange approximation was used [21,22]. In contrast to most other LSDA+DMFT implementations, within the SPR-KKR scheme, the complex and energy-dependent self-energy σ_{DMFT} is implemented as an additional energy-dependent potential to the radial Dirac equation, which is solved in order to calculate the new Green's function. This procedure is repeated until self-consistency in both the self-energy and the charge density is achieved. The double counting problem (separation of the Hubbard Hamiltonian from the LSDA one) was considered within the usual around mean-field (AMF) limit. The self-energy within the DMFT is parametrized by the average screened Coulomb interaction U and the Hund exchange interaction J. For the Fe atoms, $U_{\mathrm{Fe}} = 1.5$ eV and $J_{\mathrm{Fe}} = 0.9$ eV were used. This is an established value for bulk Fe [23]. DMFT calculations have been performed for $T = 400$ K and 4096 Matsubara poles were used to calculate the corresponding SPTF self-energy. For the treatment of off-stoichiometry compositions and the resultant chemical disorder in the $D0_3$ and $B2$ phases and the chemical disorder in the $A2$ phase, the coherent potential approximation (CPA) was applied. The CPA is considered to be the best theory among the so-called single-site (local) alloy theories that assume complete random disorder and ignore short-range order. A combination of the CPA and LSDA+DMFT within the SPR-KKR method has been used recently [20,24,25]. These calculations are referred to as CPA in this work.

In addition, for certain compositions, supercell models containing 16 atoms per unit cell were also used, and in this case, the lattice size was relaxed to find the minimum energy state. Both $D0_3$ and $B2$-like structures were investigated for $x = 0.75$. For $x = 0.625$ and $0.687\,5$, body-centered Fe atoms of the stoichiometric $D0_3$ unit cell were replaced by Si, forming off-stoichiometry $D0_3$-like structures; all the body-centered atoms were randomized to form $B2$-like structures. For $x = 0.50$, the $B2$-like and $D0_3$-like phases are identical with all Fe at cube corner sites surrounded by Si in all the body-centered sites. The lattice constants of these simulated structures were found to be within 1.5% of the experimental values. The $A2$ structure was also calculated for $x = 0.65$. The exchange-correlation functions were treated at the level of generalized-gradient approximation [26].

To support the interpretation of the experimental results, XAS spectra were calculated based on Fermi's golden rule and implemented within the SPR-KKR method; this calculation

was performed on the CPA-calculated alloys only [21,27]. For a direct comparison of the calculated absorption coefficient to experimental data, the corresponding theoretical spectra were broadened in the conventional way; Lorentzian broadening (0.3 eV) was applied to account for the lifetime of the core hole and excited electrons, and Gaussian broadening (∼0.4 eV) was used to represent finite experimental resolution.

B. Experimental procedure

Epitaxial Fe_xSi_{1-x} thin films (1000–1500 Å) in the composition range $0.55 < x < 0.77$ were grown by electron beam coevaporation of Fe and Si at 300°C on (001) MgO. Films with $x < 0.70$ did not grow epitaxially on MgO at 300 °C; for these samples, a 30-Å Cr seed layer was deposited at 200 °C, followed by the film growth at room temperature in order to obtain epitaxy while limiting interdiffusion of Cr [14]. Films intended for XAS measurements were capped with 15–18 Å of Al to prevent surface oxidation. An epitaxial $x = 1.0$ sample was also fabricated as a standard for XAS studies. Structural characterization was performed by x-ray diffraction (XRD) and high-resolution cross-section transmission electron microscopy (HRXTEM). The XRD θ-2θ scans showed only the 100 and 200 (200 and 400) peaks of the $B2$ ($D0_3$) crystal structure out of plane, and φ scans on the 110 $B2$ or 220 $D0_3$ off-axis peak showed sharp peaks (FWHM ∼2–3°) with the expected fourfold symmetry of an epitaxial film (see Ref. [7] for representative plots). The epitaxial relationship between film and substrate is Fe_xSi_{1-x} [100]|| MgO [110]. We note the 100 $B2$ and 200 $D0_3$ peaks are located at the same 2θ value since the $D0_3$ unit cell is double the size of the $B2$ (CsCl) unit cell. Scattering from the 111 planes should produce a diffraction condition for $D0_3$ but not $B2$, while diffraction from 222 planes will be present in both structures. Experimentally the intensity of the 111 XRD peak was too low to assess the chemical order, so ^{57}Fe CEMS was used as a local probe of the Fe atoms' chemical environment and the resulting atomic magnetic moment. These measurements were performed at room temperature under normal incidence, with a homemade helium-methane gas proportional counter, with ^{57}Co in a Rh matrix as the source [28]. Isomer shifts are given with respect to α-Fe at 300 K, and the spectra were fit using the histogram method [29]. Since the magnetic transition temperature for the $x = 0.55$ sample is at or below room temperature (Fig. 4), it could not investigated by CEMS. Macroscopic magnetic properties of the films were investigated with a superconducting quantum interference device (SQUID) magnetometer at temperatures from 2 to 300 K.

XAS was performed at room temperature in total electron yield (TEY) at the Fe L edges at BL 6.3.1 at the Advanced Light Source (ALS), Lawrence Berkeley National Lab, Berkeley, CA.

III. RESULTS

A. Structural characterization and chemical order

The 100 reflection in the $A2$ (bcc) structure is forbidden by structure factor cancellation but is present in both $D0_3$ and $B2$, which can be viewed (and indexed) as chemically ordered $A2$ phases. This superlattice peak is observed in all epitaxial

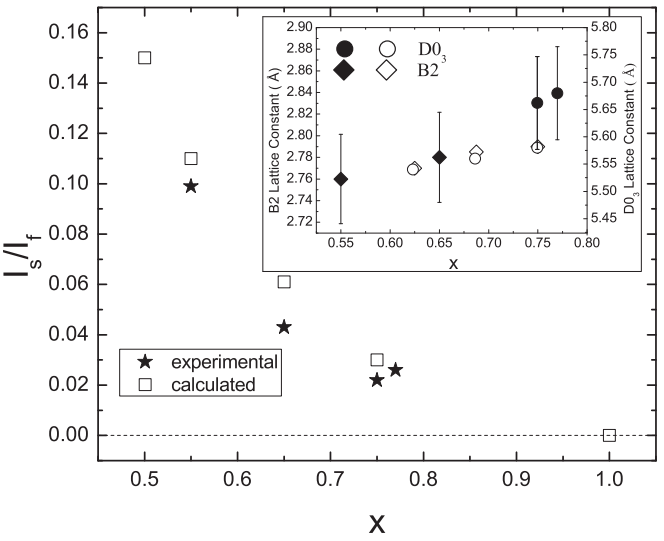

FIG. 2. Experimental and calculated superlattice (i.e., 200 $D0_3$ and 100 $B2$) to fundamental (i.e., 400 $D0_3$ and 200 $B2$) peak intensity ratios versus x. The closed (open) symbols in the inset show the measured (theoretical) lattice constant [$B2$ (left axis), $D0_3$ (right axis)] versus x, calculated from the superlattice reflection (supercell structures); $B2$ and $D0_3$ labels are based on CEMS analysis of these samples. The error bars in the inset represent an error of 1.5%.

Fe_xSi_{1-x} thin films investigated here, indicating either $B2$ or $D0_3$ order. From this peak, it is not possible to distinguish between these two types of order; the nature of the chemical ordering leads to the same intensity for both $B2$ and $D0_3$ with the same composition. The chemical order is obtained from the intensity ratio of the superlattice to fundamental peaks. The experimental values along with those calculated for perfect chemical order, based on atomic scattering factors reported in [30], are plotted in Fig. 2 as a function of x. The ratio decreases as the Fe concentration increases, as expected since at $x = 1.0$ the reflection is forbidden. The experimental intensity ratios are close to the calculated values for perfect off-stoichiometry order, indicating the films have good chemical order. The inset of Fig. 2 is a plot of the out-of-plane lattice constant as a function of Fe concentration, calculated from the superlattice reflection (i.e., 200 $D0_3$ and 100 $B2$) in the θ-2θ x-ray diffraction patterns. The linear variation in lattice constant with x indicates the presence of a single phase and shows that the lattice constant does not depend on $B2$ versus $D0_3$ ordering, consistent with theoretical supercell calculations (also shown in the inset).

HRXTEM was performed on an epitaxial $x = 0.55$ thin film. Consistent with XRD measurements, the electron diffraction pattern shows a superlattice reflection (i.e., 100), and the bright field image and the electron diffraction pattern show the orientation between the film and the substrate is $Fe_{0.55}Si_{0.45}$ [100]|| MgO [110]. Very small regions in the bright field image indicate a small portion of the film (∼10%) is not epitaxial.

To differentiate between $D0_3$ and $B2$ phases CEMS was performed. The hyperfine (hf) field B_{hf}, isomer shift δ, and relative area of each component (A_r) are summarized for all ferromagnetic samples in Table I. The magnitude of the magnetic moment at the iron site is proportional to the

TABLE I. Values of the half-width at half-maximum (Γ), isomer shift (δ), magnetic hyperfine field (B_{hf}), and relative spectral area (A_r) of the different components (Comp.) deduced from the least-squared fit of the Mössbauer spectra of Fe_xSi_{1-x} thin films. The sample with composition $x = 0.55$ is not reported since CEMS revealed a paramagnet at room temperature.

x	Sample	Component	Γ (mm s^{-1})	δ (mm s^{-1})	B_{hf} (T)	A_r
0.77	a	1	0.17	0.259	19.4	0.49
		2	0.17	0.067	30.4	0.39
		3	0.17	0.183	24.3	0.12
0.75	b	1	0.15	0.255	20.1	0.52
		2	0.15	0.089	31.1	0.30
		3	0.15	0.164	24.6	0.11
		4	0.15	0.077	27.6	0.07
0.65	c	p	0.3	≈0	0	0.26
		m		0.141[a]	14.1[a]	0.74

[a]Spectrally weighted average value.

measured B_{hf} value of the magnetically splitted sextet, while its orientation is obtained by the relative intensity (R_{23}) of the second (fifth) line with respect to the third (fourth) line of the sextet. In normal incidence geometry, this ratio ranges between 0 and 4, corresponding to an orientation of the hf field from out-of-plane to in-plane, respectively.

The CEM spectrum obtained for $Fe_{0.77}Si_{0.23}$ [Fig. 3(a)] shows very sharp spectral lines and can be fit with three sextets with in-plane orientation of the magnetic hyperfine field that are represented next to the experimental spectrum. The first component, with a hyperfine field value of B_{hf} 19.5 T, corresponds to the Fe_{II} site in the $D0_3$ crystal structure of Fe_3Si (see Fig. 1), in good agreement with other experimental studies [8,12,31,32]. This Fe site has four Fe NN and four Si NN. The second component has a hyperfine field value of $B_{hf} = 24.3$ T, corresponding to Fe atoms at the cube edges with five Fe NN and three Si NN, since the sample is off-stoichiometry in Fe concentration [8]. The last component has a hyperfine field value of $B_{hf} = 30.6$ T, which characterizes the Fe_I site, with eight Fe NN and zero Si NN [6,8,12]. This spectrum reflects a site-selective substitution in the perfectly ordered $D0_3$ crystal structure, meaning that as Fe concentration is increased above stoichiometric Fe_3Si, the additional Fe substitutes only into the Si sites. This spectrum indicates excellent $D0_3$ chemical order in the sample.

Figure 3(b) shows the CEM spectrum for $Fe_{0.75}Si_{0.25}$. In this sample, we obtain the three aforementioned components plus one additional sextet, corresponding to the Fe_{II} site with six Fe NN [8]. Like the previous film, this one also exhibits the $D0_3$ crystal structure. Additional components (Fe with five or six Fe NN) are present in the fit to the CEMS spectra, indicating that this sample deviates from perfect $D0_3$ chemical order. Previous reports on Fe_3Si thin films grown on MgO and GaAs observed similar CEMS spectra and attributed the chemical disorder to interface effects [12]. We note that in perfectly ordered $D0_3$, for $x \geqslant 0.75$, there are no Fe with less than four Fe NN, while for $x < 0.75$, in $D0_3$, there are.

For the $Fe_{0.65}Si_{0.35}$ sample, the CEM spectrum obtained [Fig. 3(c)] is significantly different, with strong overlapping lines. We have found that the best fit is obtained with a paramagnetic component (fitted quadrupole splitting value = 0.55 mm/s) and ferromagnetic components with a wide distribution of magnetically split sextets of varying hyperfine fields and isomer shift values to take into account all the structural and chemical environments of Fe atoms. The paramagnetic and ferromagnetic components are labeled p and m, respectively, in Figs. 3(c) and Table I. From this fitting procedure, the average value of the hyperfine field is $\langle B_{hf} \rangle = 14.1$ T. These data indicate significant chemical disorder. The paramagnetic doublet is due to local atomic arrangements in which Fe atoms have no moment, which we suggest is associated with two or fewer Fe/more than six Si NN, the extreme being the nonmagnetic $B2$ phase where Fe has no Fe NN. This result is consistent with other reports, which show that Fe-Si hybridization reduces the magnetic moment and thus suggests a critical number of Fe NN required to produce a magnetic moment [8,33,34]. The distribution of hyperfine fields is due to local atomic arrangements in which Fe atoms have three or more Fe neighbors and hence a magnetic moment and hyperfine splitting [9]. The shape of the hyperfine field distribution is a double Gaussian, with peaks at 8 and 20–30 T, meaning it is not a random bcc solid solution of Fe and Si, but neither is it $D0_3$. The hyperfine fields associated with an off-stoichiometric ($0.5 < x < 0.75$) $D0_3$ structure will produce a set of sharp peaks corresponding to Fe atoms with

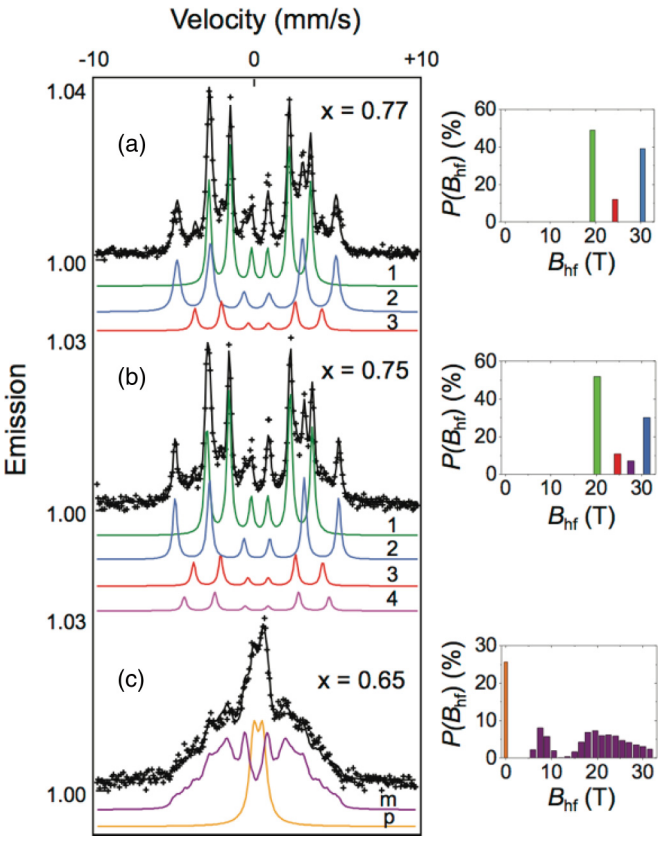

FIG. 3. (Color online) Measured CEM spectra at 293 K of epitaxial Fe_xSi_{1-x} films on MgO (001) for (a) $x = 0.77$, (b) $x = 0.75$, and (c) $x = 0.65$. The right-hand side shows the hyperfine field distribution, $P(B_{hf})$, for each sample. Corresponding least-squared fitted components (labeled 1–4; m–p) are shown below the spectra.

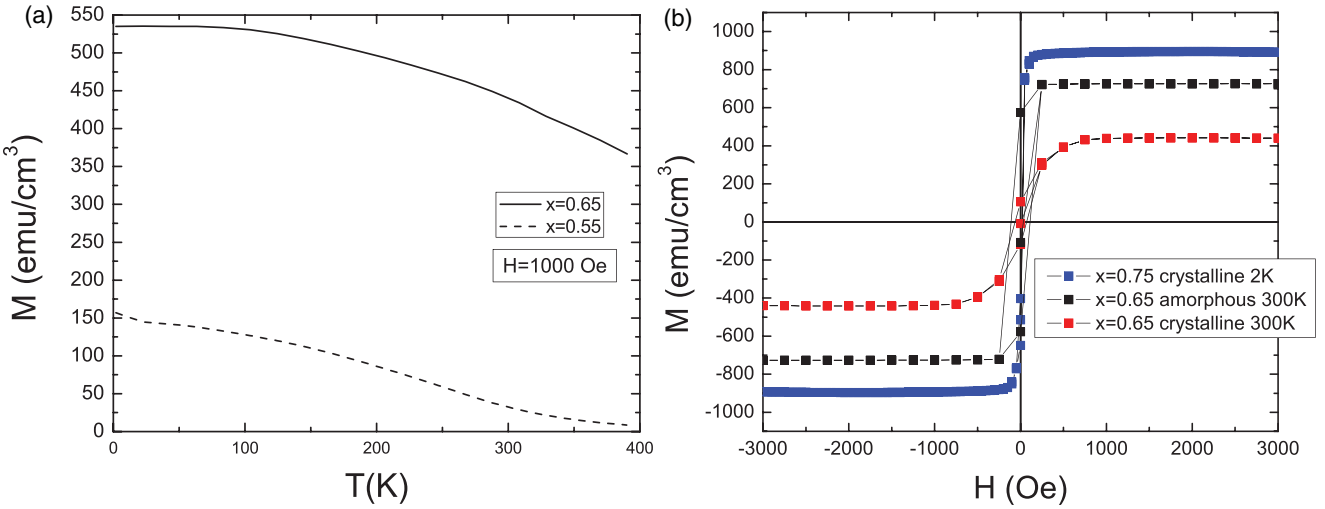

FIG. 4. (Color online) (a) M(T) for $x = 0.65$ and 0.55 at 1000 Oe and (b) M(H) for $x = 0.65$ crystalline and amorphous (from Ref. [33]) at 300 K and $x = 0.75$ crystalline at 2 K. The magnetic transition temperature for $x = 0.75$ is over 800 K [6] and therefore the difference between M(H) at 2 K and 300 K is not significant for this sample.

0–8 Fe NN (8–0 Si NN) and six Fe (Si) next nearest neighbors (NNN) for Fe_{II} (Fe_I) sites, as seen in [9]. Note that if $D0_3$ order is preserved, this statement about NN and NNN numbers is always true, even for off-stoichiometry. More specifically, while moving from $x = 0.75$–0.50, in the $D0_3$ structure, excess Si will only substitute onto Fe_I (body-centered) sites. Hence the remaining Fe_I sites will always maintain six Si NNN. By contrast in the $B2$ structure, the distinction between Fe and Si body-centered sites is lost, meaning the NNN of these body-centered sites (which are other body centers) are a distribution encompassing 0–6 Fe/6–0 Si NNN. Therefore, the broad distribution seen here is explained by disorder on the NNN sites. These many NNN environments also lead to the lack of the 33-T component found in bcc Fe with its eight Fe NN and six Fe NNN; Fe atoms with eight Fe NN but varying numbers of NNN instead produce the enhanced spectral weight between 20 and 30 T. The peak in the distribution around 8 T is due to Fe_{II} atoms (cube corners) in the $B2$ structure. This result is in agreement with the XRD pattern where a superlattice peak is observed, and the order parameter calculated experimentally (0.043 versus 0.061 theoretical, see Fig. 2) indicates that the Fe_{II} sites (cube corners) are still mostly ordered. The sample is primarily chemically disordered on the Fe_I site and thus is a $B2$ structure [35–37]. Figures 4(a) and 4(b) show M(T) with $H = 1000$ Oe for $x = 0.65, 0.55$ and M(H) for $x = 0.75$ (2 K), 0.65 (300 K) and an amorphous sample with $x = 0.65$ (300 K) from our previous work [33]. Comparison of the hysteresis loops shows that the epitaxial $x = 0.65$ sample is ferromagnetic at 300 K, where the CEMS analysis is made and saturates magnetically at approximately 800 Oe. Moreover, we note that the ratio of the weighted average of the hf field for $x = 0.75$ and 0.65 is 2.3, consistent with the calculated ratio of the saturation magnetization, 2.0.

It therefore appears that as the Fe concentration decreases below the stoichiometric $x = 0.75$, the system becomes more chemically disordered, crossing from $D0_3$ at $x = 0.75$ to the $B2$ phase (full chemical disorder on the Fe_I and Si sites, which lose their distinction) for $x = 0.65$. This chemical disorder, however, never extends to all sites (based on XRD), which would be the fully chemically disordered $A2$ phase.

B. Electronic properties

To investigate the influence of local ordering on the electronic structure, the electronic density of states (DOS) for both up (↑) and down (↓) spins for the supercell $D0_3$, $B2$, and $A2$ structures with compositions near $x = 0.65$ are shown in Fig. 5(a). Many of the sharp features in the $B2$ and $D0_3$ structures are broadened in the $A2$ structure due to increasing disorder. For instance, the peaks in the majority spin channel above the E_F in the DOS of the $D0_3$ and $B2$ structures disappear in the profile of the $A2$ structure. Moreover, the unoccupied peak in the minority spin channel at ∼0.9 eV is broadened significantly, causing an increased magnetic moment in the chemically disordered alloys. Figure 5(b) shows the spin polarization (P) calculated at E_F from $[D\uparrow(E_F) - D\downarrow(E_F)]/[D\uparrow(E_F) + D\downarrow(E_F)]$. The $B2$ value is reduced with respect to $D0_3$, and the $A2$ spin polarization is very small compared to the more chemically ordered structures. The majority charge carriers at E_F switch from spin up ($D0_3$, $B2$) to spin down ($A2$).

The electronic properties of the samples were also probed via XAS at the Fe L_2 and L_3 edges. Figure 6 shows the (a) experimental and (b) theoretical (CPA) XAS for various Fe concentrations. The $x = 1.0$ (Fe) concentration is included as a reference point, and we note that the features in the $x = 0.75$ spectrum are in agreement with previous thin-film XAS experiments for this compound [12]. To be consistent with the structures determined by CEMS, the theoretical XAS results are based on the $D0_3$ structure for $x = 0.75$ and the $B2$ structure (CPA model to account for off-stoichiometric compositions) for $x = 0.55, 0.65$. As the Si concentration increases, broadening of the L_3 edge is seen in the experimental results. Additional structure (compared to the Fe reference sample) is visible on the higher-energy side of the L_3 peak in both theory and experiment. The feature is present at a

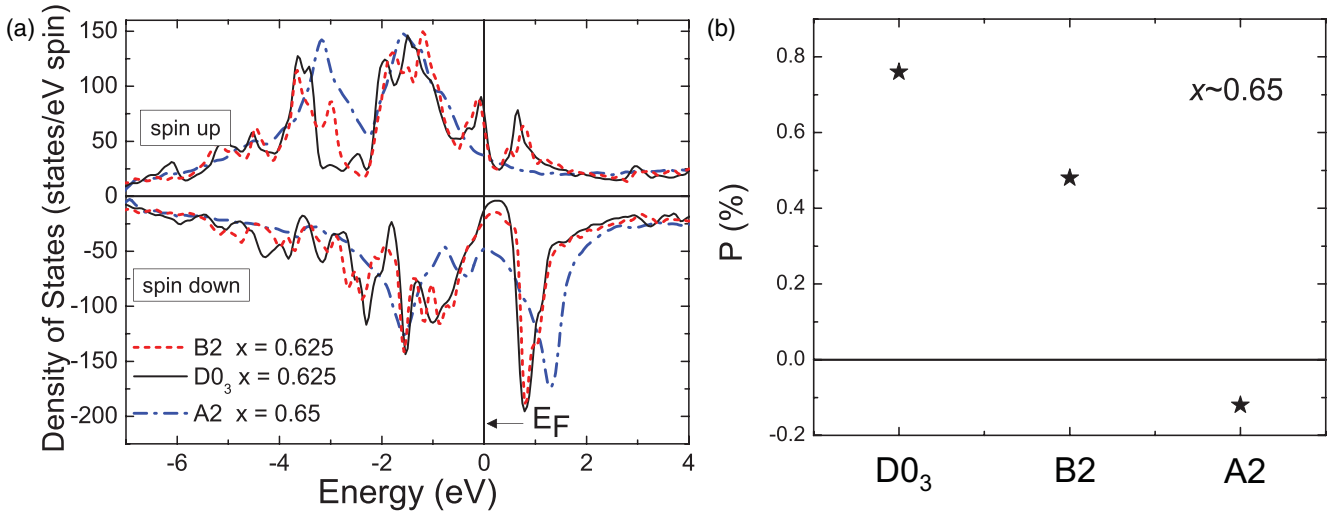

FIG. 5. (Color online) (a) Calculated density of states (supercell) for crystalline structures with various chemical order near $x = 0.65$. (b) Spin polarization P at E_F determined from the DOS in (a).

higher binding energy in the theoretical calculations than what is observed experimentally. The size of the shoulder in the experimental data increases with increasing Si concentration; for $x = 0.55$, the shoulder is not as distinct due to peak broadening. In contrast, the shoulder is clearly present for $x = 0.75$ and 0.55 but not $x = 0.65$ in the theoretical predictions. This additional feature is consistent with previous work [12] and is understood in terms of hybridization between Si s states and Fe d states at the Fe_{II} site. The presence of this shoulder in the experimental spectra indicates two chemically distinct Fe sites for all x: Fe_{II} which is hybridized with Si and Fe_I that is not, as expected for both the $D0_3$ and off-stoichiometry $B2$ structures. The CPA XAS calculation predicts the shoulder for the $x = 0.75$ composition, where the calculation accounts for two chemically inequivalent Fe sites in the $D0_3$ structure (Fe_I and Fe_{II}). However, for $x = 0.65$, while the CPA calculation includes two distinct Fe sites, to account for disorder the cube center Fe site (Fe_I) is an "average atom," which is a mix of Fe and Si to obtain the appropriate composition. Evidently this method to account for disorder does not reproduce the additional feature in the XAS spectra until the "average atom" is mostly Si (90%) at $x = 0.55$.

In a previous work, we investigated the effect of chemical disorder on the electronic structure experimentally (hard x-ray photoemission spectroscopy, HAXPES) and theoretically (CPA to account for disorder) [7]. Our results showed the chemically inequivalent Fe sites were reflected in distinct features in the valance band, consistent with the site-specific features experimentally observed here in XAS.

C. Magnetic properties

Figure 7 shows the experimentally measured saturation magnetization in μ_B/Fe (from M-H curves at 2 K) as a function of composition x. Also shown in this plot are CPA and supercell theoretical calculations of the magnetic moment for structures with different chemical order, $A2$, $B2$, and $D0_3$ as indicated. The theoretical moments (both CPA and supercell) of the $A2$ crystal structure are larger than those obtained for the $B2$ or $D0_3$ crystal structures, particularly as the Si concentration is increased. The $B2$ and $D0_3$ structures exhibit the same magnetic moment for supercell theoretical calculations and show an excellent agreement with the experimental results. Although the $D0_3$ CPA calculations near

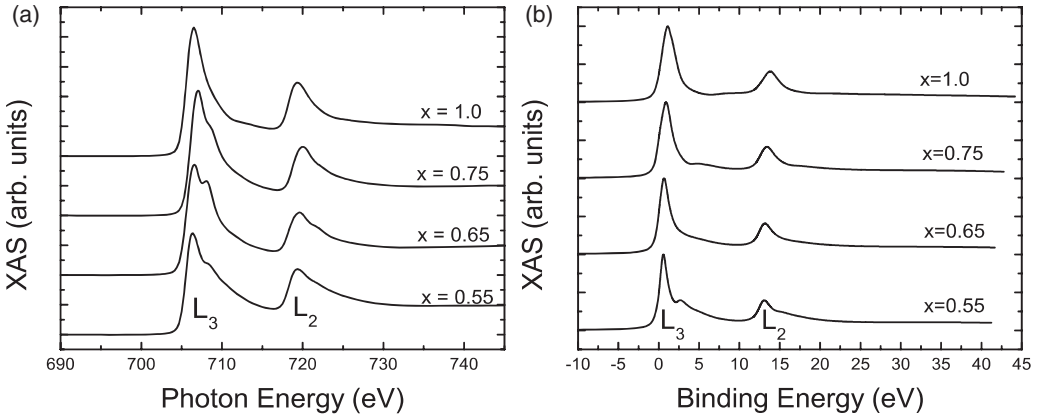

FIG. 6. X-ray absorption spectra (XAS) for Fe L-edge for $x = 0.55$–1.0. (a) Experimental results and (b) theoretical calculations based on bcc ($x = 1.0$), $D0_3$ structure (0.75), $B2$ in CPA approximation ($x = 0.65$ and 0.55).

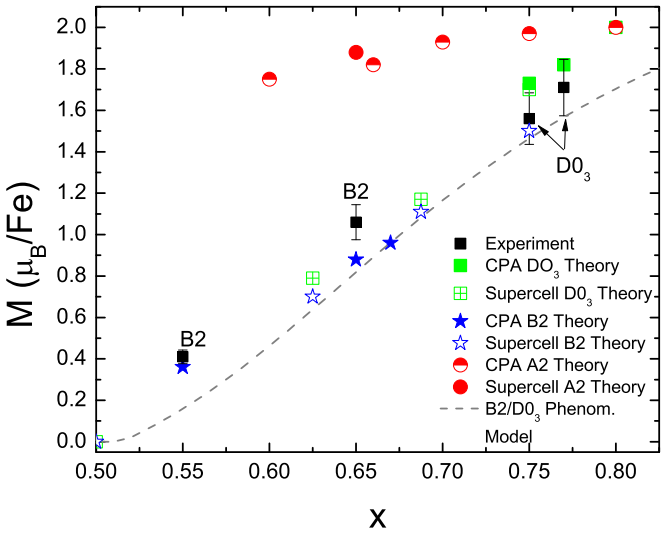

FIG. 7. (Color online) Saturation magnetization M_s vs x measured at 2 K for Fe_xSi_{1-x} epitaxial films (black squares, labeled with $B2$ or $D0_3$ based on CEMS analysis) and theoretical values for different chemical order, $A2$ (red circles), $B2$ (blue stars), and $D0_3$ (green squares) from CPA (solid symbols) and supercell (open sysmbols) calculations. Gray dashed line shows phenomenological $B2/D0_3$ model, discussed in text.

$x = 0.75$ show a slightly higher moment, they still reasonably reproduce the experimental $D0_3$ magnetic moments and are consistent with previous reports [12]. The magnetic moments of the $B2$ and $D0_3$ crystal structure should be essentially the same since the first-nearest-neighbor environments are the same; on average there is the same number of Fe-Fe (and Fe-Si) first-nearest-neighbor pairs in both structures. Only the second-nearest-neighbor environments, which apparently have a weaker effect on the magnetic moment despite their influence on the CEMS hyperfine field peak widths, are different.

In addition, the plot shows a simple phenomenological model for the $B2/D0_3$ structures, adapted from Ref. [6]. This model predicts the magnetic moment (σ_0) when additional Si (Fe) substitutes preferentially onto Fe_I (Si) sites as the concentration deviates from stoichiometric Fe_3Si. In this simple model where only nearest-neighbor interactions are taken into account, the $D0_3$ and $B2$ structures have the same magnetic moment, since the NN environments are the same, as previously discussed. Our Mössbauer results suggest a dependence of the hyperfine field on NNN type (producing a broadening in the lines due to variability in NNN for the same number of NN). This NNN effect is seen most clearly in the drop from 32 to 29 T in going from bcc Fe to $D0_3$ Fe_I (body centers), both with eight Fe NN, but the former with six Fe NNN and the latter with six Si NNN, as seen in [9]. This dependence on NNN is thus of the order of 10% and hence a relatively small perturbation in the value of the moment; it is not included in the simple phenomenological model presented here but is a source of nonlinearity in moment vs x. This model describes the data well and is consistent with the more rigorous density functional theory calculations. The magnetic moment is calculated based on Eq. (1). The moment of the Fe_{II} atoms is determined by calculating the probability of Fe nearest neighbors (P_i) and the associated magnetic moment (μ_i), which are defined in Eqs. (2) and (3), respectively. P_i is the probability for an Fe atom in any of eight sites of the bcc crystal structure to have i Fe NN. In Eq. (2), n is defined as the number of sites available, m the number of Fe nearest neighbors, and c the concentration of Fe in the film. μ_i is the magnetic moment associated with i Fe nearest neighbors, determined using the ratio of the hyperfine fields (H_i/H_8) obtained experimentally from either NMR or Mössbauer spectroscopy on bulk samples in [6]. Since a critical number of Fe NN are necessary to produce a magnetic moment, $(H_i/H_8) = 0$ for $i = 1,2$. For the Fe_I sites, the moment is assumed to remain constant at $2.2\,\mu_B$. Only the prefactor, which is the Fe concentration as the composition deviates from stoichiometry, varies. For Si, the moment is also held constant ($-0.07\,\mu_B$, as determined from polarized neutron experiments [6]), so its contribution is modulated only by the concentration. W_o is a prefactor that takes into account the different molecular weights of Fe and Si using a weighted average (i.e., $W_o = 1$ when $x = 1$ and $W_o = 2$ when $x = 0$). y is defined in $Fe_{75-y}Si_{25+y}$.

$$\sigma_0 = \left(\frac{223.2}{W_0}\right)\left[(25-y)(2.2) + (25+y)(-0.07) + 50\sum_{i=0}^{8} P_i\mu_i\right] \quad (1)$$

$$P_i = \left(\frac{n!}{m!(n-m)!}\right) c^m (1-c)^{n-m} \quad (2)$$

$$\mu_i = \left(\frac{H_i}{H_8}\right)\mu_8 \quad (3)$$

IV. DISCUSSION

Since the magnetic moment of Fe is known to be strongly dependent on the local atomic environment [6], we expect the chemical order to influence the magnetic moment in these systems. As observed recently in amorphous Fe_xSi_{1-x} thin films, Fe-Si hybridization is key to understanding the magnetic behavior of this system [33]. The magnetization was actually found to be larger in the amorphous films as compared to the crystalline counterparts, because of the reduced number of Fe-Si pairs, resulting in less Si $s-$ Fe $d-$ hybridization. The fact that the magnetization in Fig. 6 agrees well with the simple phenomenological model reflects this strong dependence on the number of Si NN around an Fe atom. The slight deviation from the model for the low-Fe-concentration $B2$ structures is due to some $A2$ disorder, which is also reflected in the order parameters calculated from XRD (Fig. 2). In a random solid solution, an Fe-Si pair is statistically less likely than in the chemically ordered structure, so the magnetic moment of the fully disordered $A2$ structure is expected to be higher than that of the $B2$ or $D0_3$ structures. As shown in Fig. 6, the theoretically predicted moment for the $A2$ structure is indeed much larger than for the $B2$ or $D0_3$ structure at the same composition, while $B2$ and $D0_3$ have the same first NN local environment and consequently the same M. The NNN environments are, however, different for $B2$ and $D0_3$,

which we showed strongly affected the hf field distribution. We suggest that the NNN broaden the distribution but do not shift the average value, explaining why the total magnetization is unaffected by these differences. This result means that some chemical disorder can be introduced into the system, and as long as the local environment does not change, the magnetic properties will remain largely unaltered.

Moreover, an analogous situation occurs when considering the electronic structure. The electronic density of states is nearly the same and the spin polarization, while reduced in the $B2$ structure, maintains the same sign as in $D0_3$. We note this result is exactly the opposite from Co_2FeSi, where introducing a small amount of disorder ($L2_1$ versus $B2$) changes the sign of the spin polarization [11]. Again, the fully chemically disordered $A2$ structure is predicted to be significantly different; the calculated DOS exhibits significant disorder broadening and the spin polarization is reduced and has a different sign.

V. CONCLUSION

The chemical order, electronic, and magnetic properties of epitaxial, off-stoichiometric Fe_xSi_{1-x} thin films ($0.50 \leqslant x \leqslant 0.77$) were investigated. This range in x allows for tuning of the magnetic and electronic properties, including the carrier concentration. The films show excellent structural (bcc-like) order and varying degrees of chemical order based on CEMS, HRXTEM, and magnetometry. $B2$ chemical order is observed for $x \leqslant 0.65$ and $D0_3$ for $x > 0.65$, possibly the result of different growth temperatures. Even far from the equilibrium compositions, $x = 0.75$ and $x = 0.5$, the films still possess significant chemical order; the $A2$ structure was never experimentally found. The theoretically calculated magnetic moments for the $B2$ and $D0_3$ structures are nearly the same and both are significantly reduced from the $A2$ moment (and the amorphous structure's moment) due to less Fe-Fe and more Fe-Si pairs. The experimental data shows that the magnetic moment is unaltered by partial chemical disorder ($B2$ phase), in good agreement with the calculations and simple model. This can be understood as due to the fact that each Fe atom has the same first-nearest-neighbor environment in the $D0_3$ and $B2$ structures, where Fe_I and Fe_{II} sites remain distinct, unlike the fully chemically disordered $A2$ phase. Interestingly, while M is clearly driven predominantly by the NN local environment, we showed that the NNN (and therefore partial chemical order) crucially affect the hf field distributions obtained from CEMS. Having many Si NNN slightly (up to 10%) reduces the average hyperfine field, and a distribution in the number of Si NNN produces broadening of the spectrum. However, partial chemical order does not significantly affect the electronic density of states, including the density of states and the spin polarization at the Fermi energy. Despite the somewhat reduced moment of these (partially) chemically ordered materials, relative to the fully disordered $A2$ or amorphous counterparts, their T_c and spin polarization remains high. These off-stoichiometric materials are easily grown and therefore offer the potential for tuning of electronic and magnetic properties, without concern about chemical disorder or the metastability of this range of concentrations, suggesting potential use in spintronic devices.

ACKNOWLEDGMENTS

This research was supported by the magnetism program at LBNL, funded by the U.S. Department of Energy (DOE), Office of Basic Energy Sciences, Division of Materials Sciences and Engineering, under Contract No. DE-AC02-05CH11231 (J.K., C.B., K.H.S., J.B.K., F.H.) and by DOE Grant No. DE-FG02-05ER46237 (Y.N.Z., J.H., R.Q.W.). Calculations were performed on parallel computers at NERSC supercomputer centers. Financial support was also provided by the German funding agencies DFG (FOR 1346) and the German ministry BMBF (05K13WMA) (J.M. and H.E.). The use of the Advanced Light Source (Berkeley, California, USA) was supported by the Director, Office of Science, Office of Basic Energy Sciences, of the United States DOE under Contract No. DE-AC02-05CH11231. We gratefully acknowledge support for x-ray absorption spectroscopy measurements from E. Arenholz and C. Jenkins, and D. J. Smith for transmission electron microscopy measurements.

[1] Y. Maeda, T. Jonishi, K. Narumi, Y. Ando, K. Ueda, M. Kumano, T. Sadoh, and M. Miyao, Appl. Phys. Lett. **91**, 171910 (2007).
[2] J. Kudrnovsky, N. E. Christensen, and O. K. Andersen, Phys. Rev. B **43**, 5924 (1991).
[3] H. Okamoto, ASM International, Alloy Phase Diagrams, 1990 [online] http://www1.asminternational.org/asmenterprise/APD/ViewAPD.aspx?id=901081.
[4] N. Manyala, Y. Sidis, J. F. DiTusa, G. Aeppli, D. P. Young, and Z. Fisk, Nature Mater. **3**, 255 (2004).
[5] S. X. Huang and C. L. Chien, Phys. Rev. Lett. **108**, 267201 (2012).
[6] D. Berling, G. Gewinner, M. C. Hanf, K. Hricovini, S. Hong, B. Loegel, A. Mehdaoui, C. Pirri, M. H. Tuilier, and P. Wetzel, J. Magn. Magn. Mater. **191**, 331 (1999).
[7] W. A. Hines, A. H. Menotti, J. I. Budnick, T. J. Burch, T. Litrenta, V. Niculescu, and K. Raj, Phys. Rev. B **13**, 4060 (1976).
[8] A. X. Gray, J. Karel, J. Minar, C. Bordel, H. Ebert, J. Braun, S. Ueda, Y. Yamashita, L. Ouyang, D. J. Smith, K. Kobayashi, F. Hellman, and C. S. Fadley, Phys. Rev. B **83**, 195112 (2011).
[9] M. B. Stearns, Phys. Rev. **129**, 1136 (1963).
[10] K. Hamaya, H. Itoh, O. Nakatsuka, K. Ueda, K. Yamamoto, M. Itakura, T. Taniyama, T. Ono, and M. Miyao, Phys. Rev. Lett. **102**, 137204 (2009).
[11] M. Pugaczowa-Michalska, A. Go, L. Dobrzynski, and S. Lipinski, J. Magn. Magn. Mater. **256**, 46 (2003).
[12] P. Bruski, S. C. Erwin, M. Ramsteiner, O. Brandt, K.-J. Friedland, R. Farshchi, J. Herfort, and H. Riechert, Phys. Rev. B **83**, 140409(R) 2011.
[13] B. Krumme, C. Weis, H. C. Herper, F. Stromberg, C. Antoniak, A. Warland, E. Schuster, P. Srivastava, M. Walterfang, K. Fauth, J. Minár, H. Ebert, P. Entel, W. Keune, and H. Wende, Phys. Rev. B **80**, 144403 (2009).

[14] K. Zakeri, I. Barsukov, N. K. Utochkina, F. M. Römer, J. Lindner, R. Meckenstock, U. von Hörsten, H. Wende, W. Keune, M. Farle, S. S. Kalarickal, K. Lenz, and Z. Frait, Phys. Rev. B **76**, 214421 (2007).
[15] M. Walterfang, W. Keune, K. Trounov, R. Peters, U. Rücker, and K. Westerholt, Phys. Rev. B **73**, 214423 (2006).
[16] S. Yamada, J. Sagar, S. Honda, L. Lari, G. Takemoto, H. Itoh, A. Hirohata, K. Mibu, M. Miyao, and K. Hamaya, Phys. Rev. B **86**, 174406 (2012).
[17] S. I. Makarov, B. Krumme, F. Stromberg, C. Weis, W. Keune, and H. Wende, Appl. Phys. Lett. **99**, 141910 (2011).
[18] S. H. Vosko, L. Wilk, and M. Nusair, Can. J. Phys. **58**, 1200 (1980).
[19] H. Ebert, D. Kodderitzsch, and J. Minar, Rep. Prog. Phys. **74**, 096501 (2011).
[20] J. Minar, J. Phys.: Condens. Matter **23**, 253201 (2011).
[21] M. I. Katsnelson and A. I. Lichtenstein, Eur. Phys. J. B **30**, 9 (2002).
[22] L. V. Pourovskii, M. I. Katsnelson, and A. I. Lichtenstein, Phys. Rev. B. **72**, 115106 (2005).
[23] J. Sanchez-Barriga, J. Fink, V. Boni, I. Di Marco, J. Braun, J. Minár, A. Varykhalov, O. Rader, V. Bellini, F. Manghi *et al.*, Phys. Rev. Lett. **103**, 267203 (2009).
[24] J. Minár, L. Chioncel, A. Perlov, H. Ebert, M. I. Katsnelson, and A. I. Lichtenstein, Phys. Rev. B **72**, 045125 (2005).
[25] O. Sipr, J. Minar, S. Mankovsky, and H. Ebert, Phys. Rev. B **78**, 144403 (2008).
[26] J. P. Perdew, K. Burke, and M. Ernzerhof, Phys. Rev. Lett. **77**, 3865 (1996).
[27] J. Minár and H. Ebert, Appl. Phys. A: Mater. Sci. Process. **78**, 847 (2004).
[28] J. Teillet, F. Varret, and J. Juraszek, MOSFIT program (unpublished).
[29] J. Juraszek, O. Zivotsky, H. Chiron, C. Vaudolon, and J. Teillet, Rev. Sci. Instrum. **80**, 043905 (2009).
[30] J. H. Hubbell, Wm. J. Veigele, E. A. Briggs, R. T. Brown, D. T. Cromer, and R. J. Howerton, J. Phys. Chem. Ref. Data **4**, 471 (1975).
[31] R. Mantovan, M. Georgieva, M. Fanciulli, A. Goikhman, N. Barantcev, Yu. Lebedinskii, and A. Zenkevich, Phys. Status Solidi A **205**, 1753 (2008).
[32] T. Shinjo, Y. Nakamura, and N. Shikazono, J. Phys. Soc. Jpn. **18**, 797 (1963).
[33] J. Karel, Y. N. Zhang, C. Bordel, K. H. Stone, C. A. Jenkins, David J. Smith, J. Hu, R. Q. Wu, S. M. Heald, J. B. Kortright, and F. Hellman, Materials Research Express **1**, 026102 (2014).
[34] Ph. Mangin and G. Marchal, J. Appl. Phys. **49**, 1709 (1978).
[35] M. Arita, S. Nasu, and F. E. Fujita, Trans. Jpn. Inst. Met. **26**, 710 (1985).
[36] E. P. Elsukov, G. N. Konygin, V. A. Barinov, and E. V. Voronina, J. Phys.: Condens. Matter **4**, 7597 (1992).
[37] K. Trunov, M. Walterfang, W. Keune, N. K. Utochkina, and A. Trunova, Thin Solid Films **516**, 6205 (2008).